Nanoscale Advances

ROYAL SOCIETY OF CHEMISTRY

PAPER

View Article Online
View Journal

Cite this: DOI: 10.1039/d5na01065a

Self-selective silver modification of SiO anodes: a conductivity-boosting strategy for high-performance lithium-ion batteries

Asif Raza,†[ac] Panjin Noh,†[a] Jaehyuk Yang,†[af] Yoon-Cheol Ha,[ae] Mukarram Ali,[a] Jae-Yeon Bang,[d] Minjoon Park, *[f] Hae-Young Choi *[ab] and Sang-Min Lee*[d]

Received 14th November 2025
Accepted 15th March 2026

DOI: 10.1039/d5na01065a

rsc.li/nanoscale-advances

Silicon-based anode materials are highly promising for next-generation lithium-ion batteries (LIBs) due to their superior theoretical capacity. However, their practical implementation is hindered by challenges such as high-volume expansion and low electrical conductivity, leading to rapid capacity degradation. In this study, we synthesized a SiO–Ag composite *via* a self-selective electroless deposition method to address these limitations. The incorporation of Ag nanoparticles significantly enhanced electrical conductivity and mitigated volume expansion, resulting in improved electrochemical performance. Structural analysis confirmed silver nano clusters distributed on SiO, facilitating efficient lithium-ion transport and charge transfer. Electrochemical evaluations demonstrated an initial coulombic efficiency of 60.9%, higher than that of pristine SiO (47.8%), along with superior cycling stability over 1000 cycles at 1C with capacity retention of 75% and enhanced rate performance. The reduced charge-transfer resistance, verified through electrochemical impedance spectroscopy, further highlights the beneficial role of Ag modification. These findings provide a viable strategy for optimizing Si-based anodes, paving the way for high-performance and durable LIBs.

1. Introduction

Lithium-ion batteries (LIBs) are extensively utilized in portable electronics and electric vehicles due to their high energy density, long cycle life, and environmental compatibility.[1] Conventional graphite anodes, despite their stability, are limited by a low theoretical specific capacity of 372 mA h g^{-1}, restricting the further improvement of energy density.[2,3] As the demand for energy storage with higher capacity grows, finding alternative anode materials with superior energy density to replace graphite has become a critical challenge. Silicon (Si), with an ultrahigh theoretical capacity (~4200 mA h g^{-1}) and suitable lithiation potential, is a promising candidate for next-generation LIB anodes.[4–6] However, its practical application is hampered by significant volume expansion (>300%) during lithiation/delithiation and poor intrinsic electrical conductivity, leading to pulverization, unstable solid electrolyte interphase (SEI) formation, rapid capacity fading, and poor rate performance.[7–10]

Silicon monoxide (SiO) has attracted attention as an alternative to pure silicon owing to its moderate theoretical capacity (~2100 mA h g^{-1}) and relatively better cycling stability.[11–14] The *in situ* formation of Li_4SiO_4 and Li_2O during initial lithiation provides a mechanically robust matrix that buffers volume fluctuations and stabilizes Si nanoclusters.[12,15] Nevertheless, SiO still suffers from sluggish Li^+/electron transport and structural instability under high current densities, resulting in limited rate capability and rapid capacity decay during long-term cycling.[16]

To overcome these challenges, significant efforts have been made to enhance electrical conductivity and cyclic stability through structural engineering and conductive modifications. Porous architectures, carbon coatings, and metal oxide shells effectively buffer volume changes and shorten Li^+ diffusion paths, improving cycling performance.[17–24] These combinations also help accommodate the volume changes during cycling, resulting in significantly improved electrochemical performance. Carbon coating is a widely adopted method to improve the electrical conductivity and accommodate volume changes in

[a]Next Generation Battery Research Center, Korea Electrotechnology Research Institute, 12, Bulmosan-ro 10 beon-gil, Seongsan-gu, Changwon-si, Gyeongsangnam-do 51543, Republic of Korea

[b]School of Chemical and Biological Engineering, Seoul National University, 1 Gwanak-ro, Gwanak-gu, Seoul 08826, Republic of Korea

[c]Department of Chemistry, University of Ulsan, TechnoSanup-ro 55-gil 12, Nam-gu, Ulsan 44776, Republic of Korea

[d]Graduate Institute of Ferrous & Energy Materials Technology (GIFT), Pohang University of Science and Technology, 77 Cheongam-Ro, Nam-Gu, Pohang, Gyeongbuk, 37673, Republic of Korea

[e]Department of Electric Energy & Materials Engineering, University of Science and Engineering (UST), Changwon 51543, Republic of Korea

[f]Department of Nano Fusion Technology, Pusan National University, Busandaehak-ro 63 beon-gil 2, Geumjeong-gu, Busan 46241, Republic of Korea

† Equal contribution: Asif Raza, Panjin Noh, Jaehyeck Yaong.

LIB electrodes.[25–28] Embedding metals within silicon-based materials has shown promise in providing additional electrical conductivity and mitigating volume expansion, offering a potential pathway to enhance the performance of SiO-based anodes in LIBs.[13,29–31] For instance, TiO_{2-x} coated porous SiO has demonstrated improved SEI stability and high-rate capability (423.4 mA h g^{-1} after 500 cycles at 2.0 A g^{-1}) due to oxygen-deficient TiO_{2-x} providing conductive pathways and a robust interfacial layer.[32] Similarly, embedding conductive metals such as silver (Ag) significantly improves electronic conductivity and mitigates stress during cycling. Ag nanoparticles, when uniformly dispersed within SiO or Si matrices, reduce charge transfer resistance and accelerate Li^+ diffusion, resulting in superior reversible capacity and rate performance.[30,33]

Silver-modified SiO composites have proven to be an effective approach, with Ag providing efficient electron conduction that improves the electrical conductivity of the material. For example, Si/Ag@SiO_x and P-SiNPs/Ag@C anodes exhibited remarkable rate performance (1099 mA h g^{-1} at 2 A g^{-1}) and excellent long-term cycling stability (706 mA h g^{-1} after 300 cycles at 1 A g^{-1}), attributed to the conductive Ag network and porous structure suppressing SiO pulverization.[33,34] Building on these advances, this study explores a self-selective electroless (galvanic displacement) deposition strategy that fundamentally differs from conventional metal-decoration approaches. Through a spontaneous redox-driven process conducted under mild conditions, Ag nanoclusters are nucleated and directly anchored onto the SiO surface without the need for external reducing agents, high-energy ball milling, template-assisted synthesis, or multi-step carbonization treatments. Importantly, this deposition process simultaneously induces controlled surface etching, leading to the generation of additional porosity. As a result, a coupled structural evolution occurs: (i) formation of a surface-anchored conductive Ag network and (ii) development of ion-accessible porous pathways. This integrated conductive-porous architecture enhances electronic transport and electrolyte infiltration concurrently, rather than addressing these factors independently. Consequently, the SiO–Ag composite exhibits improved charge-transfer kinetics (lower interfacial resistance and reduced Warburg impedance), enhanced apparent Li^+ diffusion behavior, and stable long-term cycling performance at 1C. Therefore, the significance of this work lies in the process–structure–transport integration enabled by the self-selective electroless route, rather than in the mere addition of Ag.

2. Experimental section

2.1 Materials synthesis

All reagents were of analytical grade and used without further purification. Commercial silicon monoxide (SiO, 99.8%, ~10 μm, Alfa Aesar) was employed as the starting material. 2 grams of SiO powder were dispersed in 2 M hydrofluoric acid (HF) and treated for 20 minutes. Subsequently, 10 mM silver nitrate ($AgNO_3$) solution was introduced into the suspension at room temperature, followed by stirring for certain time to facilitate the deposition of silver on the SiO surface by galvanic displacement reaction. The resulting product was filtered, thoroughly washed with deionized water to remove residual silver precursors, and dried in a vacuum oven at 100 °C overnight. The obtained material was designated as SiO–Ag.

2.2 Materials characterization

The crystal structure of the powders was examined using X-ray diffraction (XRD) with a Rigaku instrument (X'pert Philips PMD, Cu Kα radiation, $\lambda = 1.5406$ Å). The surface morphology and chemical composition were studied using a field-emission scanning electron microscope (FE-SEM, Hitachi S-4800). Specific surface areas, pore sizes, and pore volumes of the samples were determined using the Brunauer–Emmett–Teller (BET) method with Quantachrome instruments (Autosorb-iQ and Quadrasorb SI). X-ray photoelectron spectroscopy (XPS) spectra were obtained using a ThermoFisher (NEXSA) microfocused monochromatic X-ray system.

2.3 Electrochemical measurements

Electrochemical tests were conducted using CR2025-type half-coin cells, which were assembled in an argon-filled glove box with moisture and oxygen levels below 0.1 ppm. Lithium metal foil (500 μm thick) served as both the counter and reference electrode. The working electrodes were prepared by coating a slurry of active material (SiO, SiO–Ag), conductive additive (Super P), and binders (carboxymethyl cellulose (CMC) and polyacrylic acid (PAA)) in a mass ratio of 80 : 5 : 7.5 : 7.5, respectively, on 10 μm thick copper foil. The loading of active material was controlled in the range of 1.1–1.2 mg cm^{-2} for all electrodes. The coated copper foils were dried at 100 °C for 6 hours and subsequently cured under vacuum at 150 °C for 1 hour. The electrodes, with a diameter of 14 mm, were punched, welded onto spacers, and vacuum-dried at 110 °C for 12 hours before assembly. The electrolyte consisted of 1.3 M $LiPF_6$ dissolved in a mixture of ethylene carbonate (EC) and diethyl carbonate (DEC) (3 : 7 v/v) with 10 wt% fluoroethylene carbonates (FEC) as an additive and a commercial polyethylene (PE) separator of thickness 16 μm was used. Galvanostatic charge–discharge measurements were conducted using a TOSCAT-3100 battery cycler (TOYO ENGINEERING CORPORATION) within a voltage window of 0.005–1.5 V *vs.* Li/Li^+. Pre-cycling was carried out at 0.05C for one cycle for initial coulombic efficiency and 0.1C for two cycles within a voltage range of 0.005–2.0 V. Afterward, the cells were cycled at a constant current density of 0.5C (1.0C = 1500 mA g^{-1}). Rate capability tests were performed at current densities ranging from 0.1C to 5.0C. Cyclic voltammetry (CV) was conducted using a Biologic VSP-200 potentiostat, with a scan rate of 0.05 mV s^{-1}, across a voltage range of 0.005–2.0 V *versus* Li/Li^+. The AC impedance measurements were conducted with an amplitude of 5 mV over the frequency range of 10 mHz to 1 MHz before cycling.

3. Results and discussion

Fig. 1 illustrates the structural and crystalline characteristics of the SiO–Ag composite. In Fig. 1a, a schematic illustration

depicts the synthesis of the SiO–Ag composite *via* a self-selective electroless deposition process eqn (1). Commercial SiO (alpha) powder was dispersed in 2 M hydrofluoric acid (HF) for 20 minutes. Subsequently, 10 mM silver nitrate ($AgNO_3$) was added, and the suspension was stirred at room temperature for 5 minutes to facilitate silver deposition (optimal sample, see SI, Fig. S1). The resulting mixture was filtered, thoroughly rinsed with deionized water to remove residual silver precursors, and dried overnight in a vacuum oven at 100 °C, yielding the SiO–Ag composite.

$$Si + 4Ag^{+} + 6F^{-} \rightarrow SiF_6^{2-} + 4Ag\downarrow \quad (1)$$

During the galvanic displacement process in the HF-containing solution, partial surface dissolution of SiO occur, potentially forming soluble hexafluorosilicate species.[35] In our system, this controlled etching is beneficial, as it generates additional surface porosity that improves electrolyte accessibility and Li^+ transport. At the same time, Ag nanoclusters nucleate on the SiO surface, forming conductive pathways.[36,37] However, excessive etching could increase side reactions; therefore, deposition time was carefully optimized to balance porosity generation and structural stability.

Fig. 1b presents the X-ray diffraction (XRD) patterns of the SiO and SiO–Ag samples. The SiO sample exhibits a broad peak, characteristic of an amorphous structure, while the SiO–Ag sample displays additional sharp peaks corresponding to crystalline silver (marked by ●). These results confirm the successful incorporation of crystalline Ag nanoparticles on SiO.

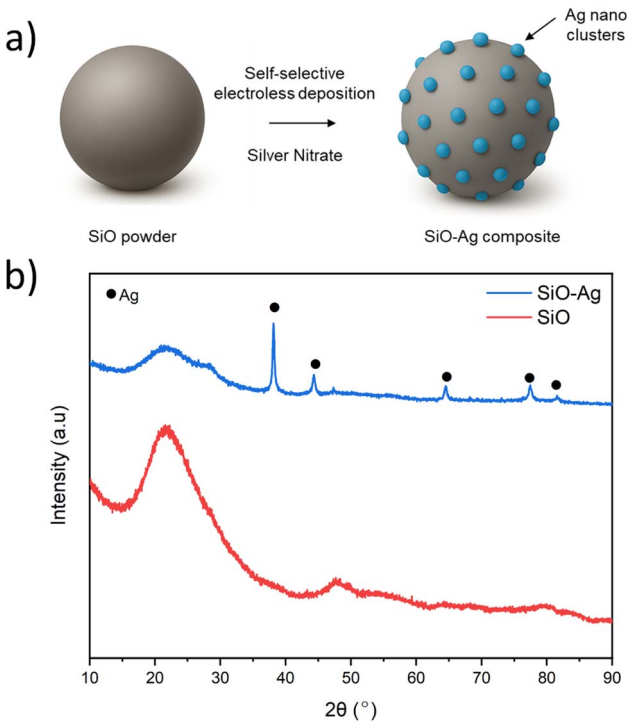

Fig. 1 (a) Synthesis schematic for SiO–Ag. (b) XRD spectra for SiO and SiO–Ag.

Fig. 2a and b, shows scanning electron microscopy (SEM) images illustrating the morphological differences between SiO (Fig. 2a) and SiO–Ag (Fig. 2b) samples. Fig. 2a reveal the smooth and compact surface morphology of SiO, with no porosity. In contrast, Fig. 2b highlights the significant structural changes in SiO–Ag upon silver incorporation. The SiO–Ag sample exhibits a porous structure with evenly distributed silver particles visible as bright spots account for 16.24 wt% (Fig. S2). These Ag-particles are well-embedded on the SiO, suggesting effective integration of silver. The enhanced porosity and uniform distribution of silver contribute to improved surface area and facilitate better ionic and electronic conductivity, which are critical for enhancing the electrochemical performance of the composite material.[38,39] This morphological transformation underscores the role of silver in altering the microstructure of SiO to create a more electrochemically favorable architecture.

Table 1, Fig. 2c and d, illustrate the nitrogen adsorption–desorption isotherms and pore size distribution curves for SiO and SiO–Ag, highlighting their textural properties. The SiO sample exhibits a surface area of 0.54 $m^2\ g^{-1}$, a pore volume of 0.0017 $m^3\ g^{-1}$, and an average pore diameter of 4.7 nm. In contrast, the SiO–Ag composite demonstrates a significantly enhanced surface area of 6.16 $m^2\ g^{-1}$, a pore volume of 0.025 $m^3\ g^{-1}$, and an average pore diameter of 13.95 nm. The nitrogen adsorption–desorption isotherms (Fig. 2c) show a marked increase in the adsorption volume for SiO–Ag at higher relative pressures, indicating the development of a mesoporous structure upon HF treatment and the incorporation of silver. Similarly, the pore size distribution (Fig. 2d) reveals that SiO–Ag possesses a broader pore size range, centered around 13.95 nm, compared to the smaller and less pronounced pores of SiO. These results suggest that the introduction of silver not only enhances the surface area and pore volume but also promotes the formation of larger pores, which are beneficial for improving electrolyte accessibility and ion diffusion during electrochemical processes.[40]

Fig. 3 presents the X-ray photoelectron spectroscopy (XPS) analysis of SiO and SiO–Ag samples, revealing their elemental composition and chemical states. Fig. 3a shows the wide-scan XPS spectra of SiO and SiO–Ag highlight the distinct elemental features of the samples. For SiO, peaks corresponding to Si 2p, Si 2s, and O 1s are observed, consistent with the silicon and oxygen composition of the material. In the SiO–Ag spectrum, additional peaks attributed to Ag 3d confirm the successful incorporation of silver into the composite. The presence of C 1s in both spectra likely arises from surface contamination. Fig. 3b shows the high-resolution O 1s spectrum of SiO–Ag displays a deconvolution into two distinct peaks located at 532.49 eV and 535.29 eV, corresponding to oxygen species. The peak at 532.49 eV is attributed to Si–O bonds,[34] while the higher binding energy peak at 535.29 eV may indicate oxygen associated with surface adsorbed species or defects[41] which does not appears in SiO sample (Fig. S3a). These features confirm the presence of oxygen-related functionalities within the SiO matrix. Fig. 3c shows the high-resolution Si 2p spectrum for SiO–Ag reveals the coexistence of multiple silicon oxidation states. Peaks corresponding to Si^0, Si^+, Si^{2+}, Si^{3+}, and Si^{4+} are

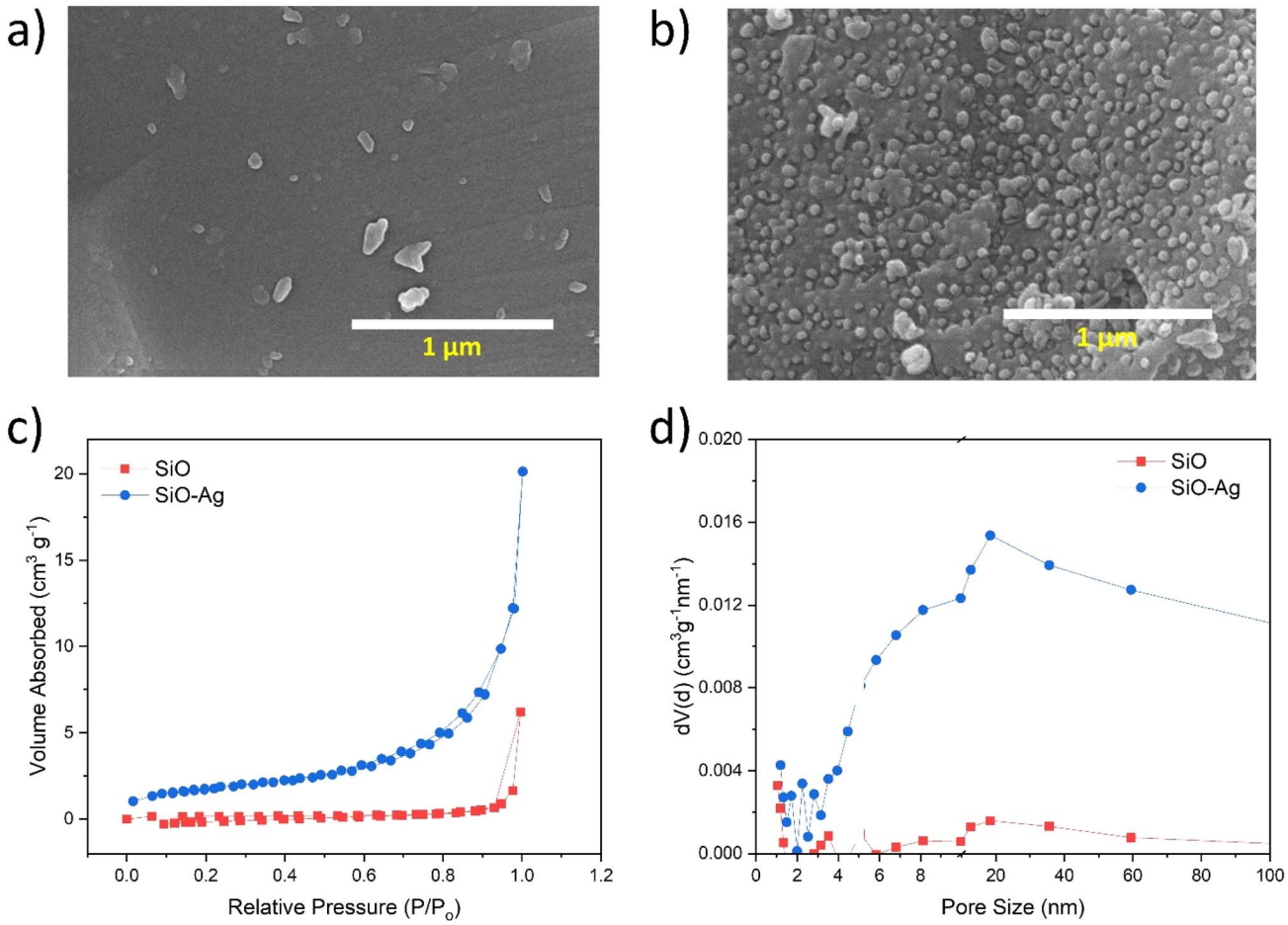

Fig. 2 SEM images for (a) SiO and, (b) SiO–Ag. BET isotherm (c) and pore size distribution (d) for SiO and SiO–Ag samples.

Table 1 Surface areas based on the Brunauer–Emmett–Teller (BET) method, pore volume, and average pore diameter of SiO and SiO–Ag composite

Sample	Surface area ($m^2\ g^{-1}$)	Pore volume ($m^3\ g^{-1}$)	Pore diameter (nm)
SiO	0.54	0.0017	4.7
SiO–Ag	6.16	0.025	13.95

observed, demonstrating the presence of silicon in varying degrees of oxidation within the composite. SiO (Fig. S3b) exhibits similar oxidation states, confirming that the incorporation of Ag into SiO does not alter its composition. This observation aligns with the results obtained from the XRD analysis. Fig. 3d shows Ag 3d spectrum for SiO–Ag sample confirms the presence of metallic silver. The two peaks at 368 eV and 374 eV correspond to Ag $3d_{5/2}$ and Ag $3d_{3/2}$, respectively, with a spin–orbit splitting of 6 eV, indicative of metallic silver. This result confirms that silver is incorporated in its metallic state,[42] which is critical for enhancing the electrical conductivity of the composite. The XPS analysis confirms the successful integration of silver onto the SiO surface. The coexistence of metallic silver and various silicon states contributes to the improved conductivity and electrochemical performance of the SiO–Ag composite. These results provide valuable insights into the chemical composition and bonding environment, essential for understanding the material's enhanced functionality.

Fig. 4 illustrates the electrochemical performance of SiO and SiO–Ag samples using coin cell, showcasing their cyclic voltammetry, charge–discharge profiles, cycling stability, and rate capabilities. Fig. 4a, presents the cyclic voltammetry (CV) profiles of SiO and Ag-doped SiO (SiO–Ag) electrodes, recorded in the voltage range of 0.01 to 3.0 V *vs.* Li/Li^+, providing insights into their electrochemical behavior. Both electrodes exhibit a broad cathodic peak below 0.5 V, corresponding to the lithiation of SiO to form Li_xSi and the decomposition of electrolyte, leading to SEI (solid electrolyte interphase) formation. The anodic peaks observed around 0.3–0.6 V represent the delithiation process of Li_xSi. Notably, the SiO–Ag electrode exhibits sharper and more pronounced current responses compared to the pristine SiO, indicating improved electrochemical reversibility and faster redox kinetics. The higher peak intensity and steeper slope of the redox peaks in the SiO–Ag sample suggest enhanced conductivity, likely attributed to the introduction of highly conductive silver nanoparticles. This improvement facilitates more efficient charge transfer during the

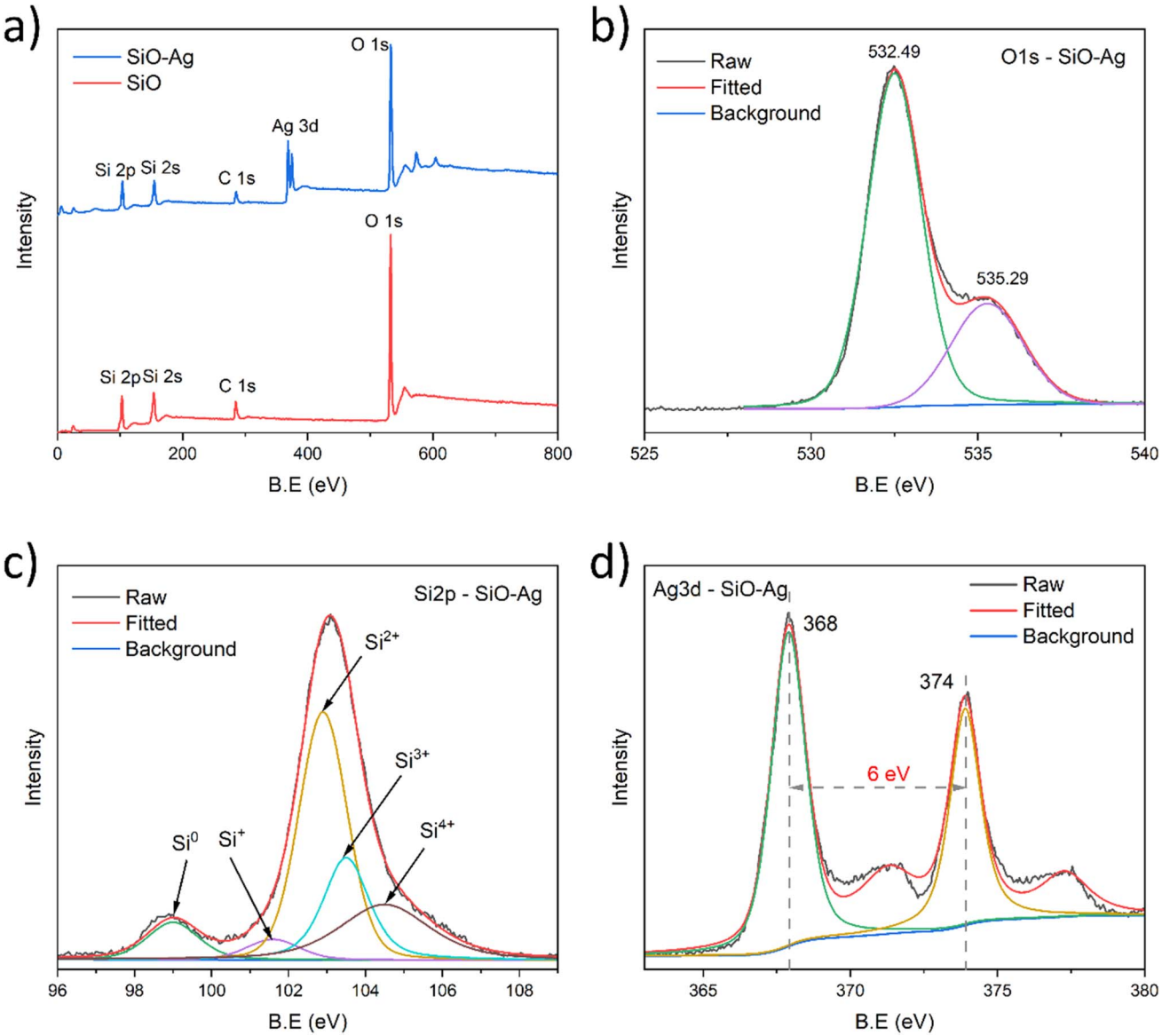

Fig. 3 (a) XPS full spectra for SiO and SiO–Ag. (b) O 1s, (c) Si 2p and, (d) Ag 3d spectra for SiO–Ag sample.

electrochemical reaction, consistent with the enhanced cycling and rate performance observed in earlier galvanostatic tests. Thus, Ag doping significantly boosts the electrochemical activity of the SiO-based anode material. In Fig. 4b, the charge and discharge capacities are shown to be significantly higher for SiO–Ag (2050.52 mA h g^{-1} and 1249.17 mA h g^{-1}, respectively), compared to SiO (1868.58 mA h g^{-1} and 892.89 mA h g^{-1}), resulting in initial coulombic efficiencies (ICE) of 47.8% for SiO and 60.9% for SiO–Ag. Fig. 4c demonstrates the long-term cycling stability, where SiO–Ag exhibits superior capacity retention of 78% after 300 cycles, compared to 51% for SiO at 0.5C (1C = 1500 mA g^{-1}). The first decay in the capacities of samples is due to the volume expansion effect of silicon particles in the cycling process. The repetitive volume changes could fracture the SEI layers and result in a more extensive exposure of Si active sites during the lithiation process. The fresh active site could provide more sites to store charge, thereby increasing capacity after few initial cycles.[12,13] It should be noted that the specific capacities reported in this study are normalized to the total mass of active material, including the Ag component in the SiO–Ag composite (≈16 wt%). Although Ag does not significantly contribute to Li storage within the investigated voltage range, its incorporation enhances electronic conductivity and charge-transfer kinetics. To further confirm the effect of Ag on SiO, Ag was selectively removed using a solution containing 1 mole of HF and 0.06 moles of H_2O_2. The electrochemical performance of the samples before and after Ag removal was evaluated and is presented in Fig. S4a. While Pitch has been utilized as a carbon source for coating SiO anodes, our current work identifies limitations in its suitability for SiO materials (Fig. S4b). Carbon coatings serve a similar purpose by providing a conductive network that mitigates the effects of SiO's volume

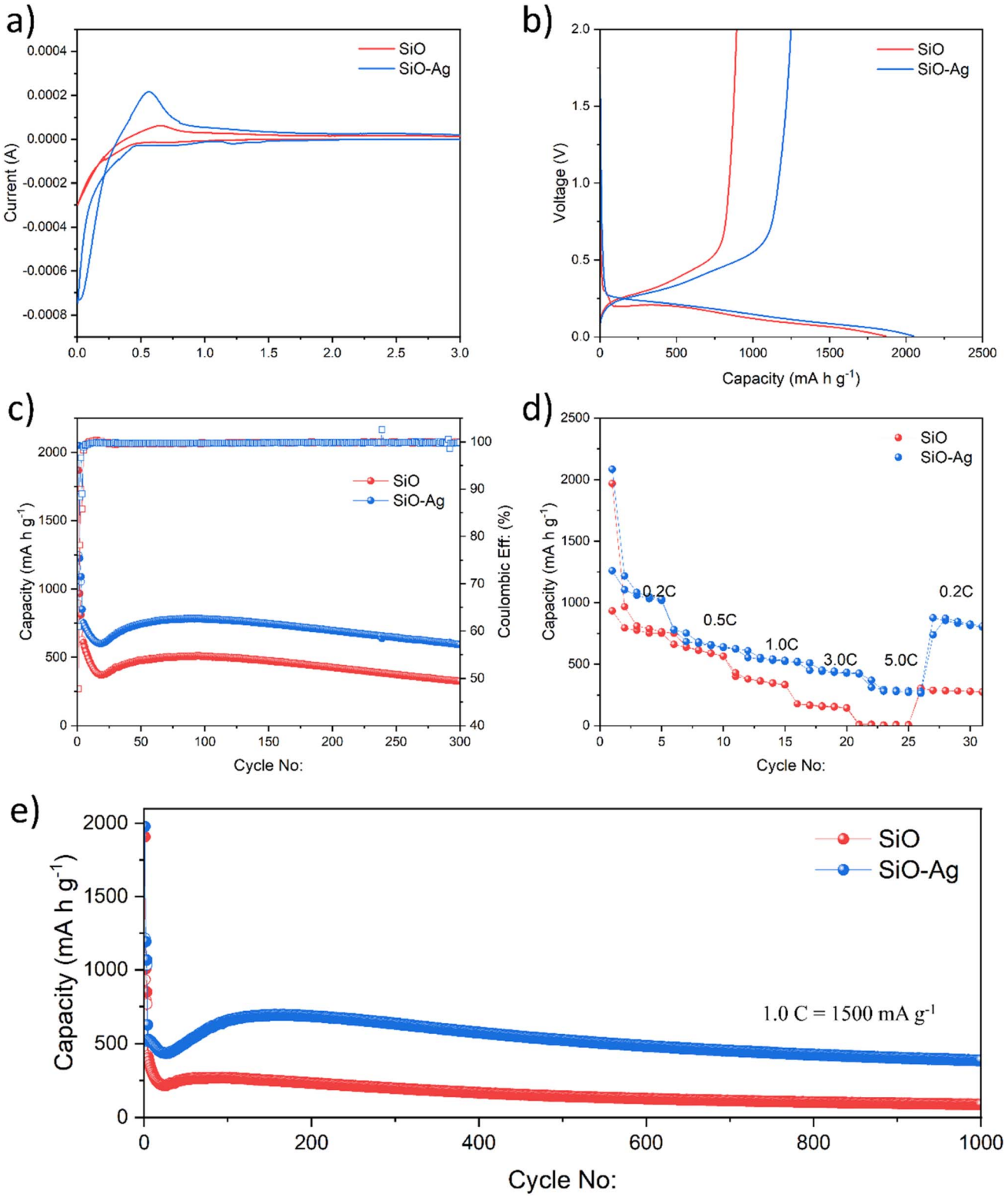

Fig. 4 Comparison of electrochemical performance for SiO and SIO–Ag, (a) Cyclic voltammetry, (b) galvani first charge/discharge at 0.05C, (c) cyclic performance at 0.5C, (d) rate capability and, (e) long-term cyclic performance at high C-rate of 1.0C.

expansion during cycling. However, as previously discussed, the application of carbon coatings on SiO anodes must be carefully optimized to balance conductivity enhancement with potential drawbacks such as reduced capacity and increased first-cycle irreversible capacity.[43] Results demonstrate that Ag doping significantly improves the cycling stability. The rate

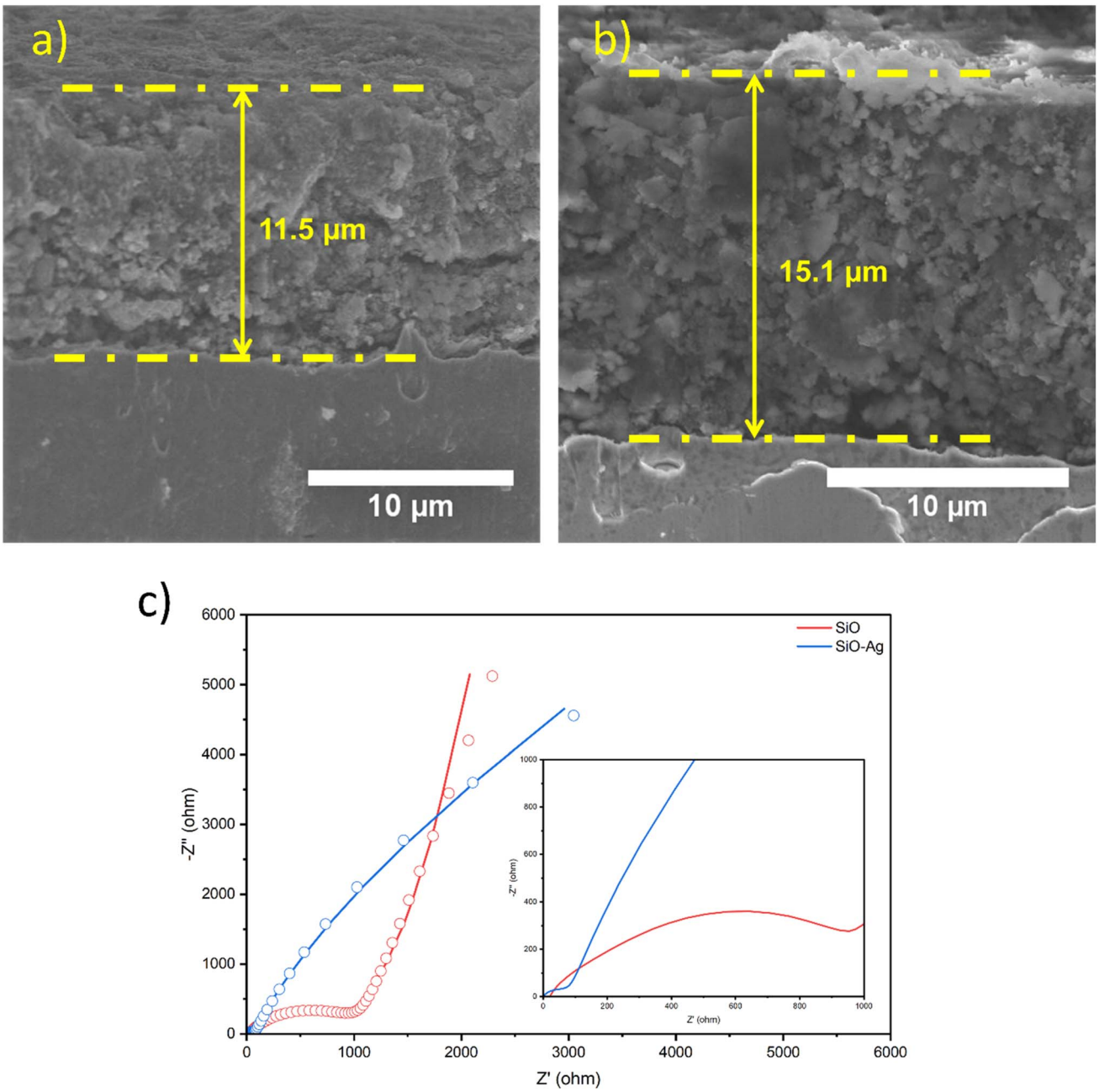

Fig. 5 Cross-section SEM images of SiO–Ag composite electrodes (a) before and (b) after cycling. (c) EIS result of SiO and SiO–Ag composite electrodes before cycling.

performance, as depicted in Fig. 4d, reveals that SiO–Ag outperforms SiO across various current densities, with specific capacities of 1105, 775, 553, 450, and 312 mA h g^{-1} at 0.2C, 0.5C, 1.0C, 3.0C, and 5.0C, respectively, and recovers to 877 mA h g^{-1} when returned to 0.2C which is marginally lower than the initial value, possibly attributed to partial material degradation induced by high-rate cycling. In comparison, SiO shows lower capacities of 933, 660, 381, 168, and 12 mA h g^{-1} at the same rates, with only 286 mA h g^{-1} upon recovery. Fig. 4e, illustrates the cycling performance of the anodes at a high current density of 1.0C. After 1000 cycles, the SiO–Ag anode retains a reversible capacity of 386 mA h g^{-1}, corresponding to approximately 75% capacity retention for 1C compared at 3rd cycle after 2 formation cycles. In contrast, the SiO anode shows significantly lower performance, with only 10% capacity retention over the same period. Comparative studies of the SiO_2 carbon composites are listed in a separate table in SI (Table S1). Furthermore, Fig. 5a and b, displays cross-sectional SEM images of the SiO–Ag electrode (a) before and (b) after long-term electrochemical cycling. Initially, the electrode thickness is approximately 11.5 μm, with a relatively compact microstructure. After cycling, the electrode expands to about 15.1 μm, indicating significant structural

changes. This increase in thickness and the more porous morphology suggests volume expansion and mechanical stress induced by repeated lithiation/delithiation processes. Despite the expansion, the electrode maintains good structural integrity and preserving electrode stability during prolonged cycling. These results highlight the enhanced electrochemical performance of SiO–Ag, attributed to the improved conductivity and structural stability imparted by pore generation Ag doping.[40]

Fig. 5c presents the Nyquist plot with fitting, illustrating the effect of Ag incorporation on the electrochemical impedance of SiO. The plot depicts the imaginary impedance (Z'') on the y-axis *versus* the real impedance (Z') on the x-axis. The semicircle appearing at high-to-mid frequencies represents the surface (R_s) and film resistance (R_f), while the semicircle in the low-frequency region corresponds to the charge-transfer resistance (R_{ct}) at the electrode–electrolyte interface.[44,45] The low-frequency straight-line segment indicates Warburg impedance, which is related to ion diffusion within the electrolyte or electrode material. Compared to SiO, the SiO–Ag composite exhibits lower $R_{s\ and}\ R_f$ and a smaller semicircle, signifying reduced surface and charge-transfer resistance. Additionally, the steeper slope in the Warburg region suggests enhanced ionic diffusion. The incorporation of Ag improves the composite's electrical conductivity, promoting more efficient charge transfer at the electrode–electrolyte interface. This improvement in ionic diffusion may be attributed to a more interconnected network structure or reduced particle agglomeration facilitated by Ag. This enhancement is further supported by the calculated lithium-ion diffusion coefficients, which are significantly improved for SiO–Ag (2.2×10^{-7} cm^2 s^{-1}) compared to pristine SiO (2.5×10^{-9} cm^2 s^{-1}) Table S2 and Fig. S5. This two-orders-of-magnitude increase in D_Li^+ confirms that Ag facilitates faster ion transport, likely due to a more conductive and interconnected network or reduced particle agglomeration. Overall, the SiO–Ag composite demonstrates superior electrochemical performance compared to pure SiO, primarily due to the synergistic effect of Ag, which enhances charge-transfer kinetics and ion transport.

4. Conclusion

In this study, we successfully synthesized a SiO–Ag composite using a self-selective electroless deposition method, demonstrating its potential as an anode material for lithium-ion batteries. The incorporation of Ag significantly enhanced electrical conductivity and mitigated volume expansion, resulting in improved electrochemical performance. Structural and morphological analyses confirmed the formation of a porous SiO with well-dispersed Ag nanoparticles, promoting better lithium-ion diffusion and charge transfer. Electrochemical tests revealed a superior initial coulombic efficiency of 60.9%, compared to 47.8% for pristine SiO at 0.1C and better capacity retention of 75% at 1C for SiO–Ag composite. The SiO–Ag composite also exhibited enhanced cycling stability, maintaining a higher capacity retention of 75% for 1 after 1000 prolonged cycling. Additionally, rate capability tests confirmed its ability to sustain high specific capacities at elevated current densities. These findings provide valuable insights into the development of high-performance anode materials. Future studies may focus on further optimizing Ag content and exploring scalable fabrication techniques for commercial applications based on full-cell integration, involving pre-lithiation and electrolyte optimization to address lithium inventory loss.

Conflicts of interest

There are no conflicts to declare.

Data availability

All data supporting the findings of this study, including XRD, XPS, SEM, BET, and electrochemical measurement results, are provided in the supplementary information (SI) of this article. Additional raw data are available from the corresponding author upon reasonable request. Supplementary information: SEM images and EDX mapping of SiO–Ag electrodes with various deposition times, XPS spectra for SiO, electrochemical cycling data comparing SiO–Ag with other SiO-based anodes, and equivalent circuit fitting data for impedance analysis. It also provides comprehensive tables comparing the electrochemical performance and lithium-ion diffusion coefficients (D_{Li+}) of the synthesized materials with previously reported literature. See DOI: https://doi.org/10.1039/d5na01065a.

Acknowledgements

This research was supported by the National Research Council of Science & Technology (NST) grant by the Korea government (MSIT) (No. GTL24011-000), and was supported by a 'Regional innovation mega project' program through the Korea Innovation Foundation funded by Ministry of Science and ICT (Project Number: 2023-DD-UP-0332) and by Korea Institute for Advancement of Technology (KIAT) grant funded by the Korea Government (MOTIE) (RS-2024-00419413, HRD Program for Industrial Innovation).

References

1 M. Armand, P. Axmann, D. Bresser, M. Copley, K. Edström, C. Ekberg, D. Guyomard, B. Lestriez, P. Novák and M. Petranikova, *J. Power Sources*, 2020, **479**, 228708.
2 T. Chen, J. Wu, Q. Zhang and X. Su, *J. Power Sources*, 2017, **363**, 126–144.
3 S. Wu, Y. Han, K. Wen, Z. Wei, D. Chen, W. Lv, T. Lei, J. Xiong, M. Gu and W. He, *Composites, Part B*, 2019, **161**, 369–375.
4 H. Zhao, J. Li, Q. Zhao, X. Huang, S. Jia, J. Ma and Y. Ren, *Electrochem. Energy Rev.*, 2024, **7**, 11.
5 M. K. Majeed, R. Iqbal, A. Hussain, M. U. Majeed, M. Z. Ashfaq, M. Ahmad, S. Rauf and A. Saleem, *Crit. Rev. Solid State Mater. Sci.*, 2024, **49**, 221–253.
6 G. F. I. Toki, M. K. Hossain, W. U. Rehman, R. Z. A. Manj, L. Wang and J. Yang, *Ind. Chem. Mater*, 2024, **2**, 226–269.

7 M. W. Verbrugge, D. R. Baker, X. Xiao, Q. Zhang and Y.-T. Cheng, *J. Phys. Chem. C*, 2015, **119**, 5341–5349.
8 J.-S. Bridel, T. Azais, M. Morcrette, J.-M. Tarascon and D. Larcher, *Chem. Mater.*, 2010, **22**, 1229–1241.
9 T. Yoon, C. C. Nguyen, D. M. Seo and B. L. Lucht, *J. Electrochem. Soc.*, 2015, **162**, A2325.
10 S. Guo, H. Li, Y. Li, Y. Han, K. Chen, G. Xu, Y. Zhu and X. Hu, *Adv. Energy Mater.*, 2018, **8**, 1800434.
11 J. Wang, H. Zhao, J. He, C. Wang and J. Wang, *J. Power Sources*, 2011, **196**, 4811–4815.
12 A. Raza, S. Y. Kim, J.-H. Choi, J.-S. Kim, M.-S. Park and S.-M. Lee, *Int. J. Energy Res.*, 2022, **46**, 18269–18277.
13 A. Raza, J. Y. Jung, C.-H. Lee, B. G. Kim, J.-H. Choi, M.-S. Park and S.-M. Lee, *ACS Appl. Mater. Interfaces*, 2021, **13**, 7161–7170.
14 Y. Hwa, C.-M. Park and H.-J. Sohn, *J. Power Sources*, 2013, **222**, 129–134.
15 X. Meng, H. Huo, Z. Cui, X. Guo and S. Dong, *Electrochim. Acta*, 2018, **283**, 183–189.
16 A. Casimir, H. Zhang, O. Ogoke, J. C. Amine, J. Lu and G. Wu, *Nano Energy*, 2016, **27**, 359–376.
17 A. Reyes Jiménez, R. Klöpsch, R. Wagner, U. C. Rodehorst, M. Kolek, R. Nölle, M. Winter and T. Placke, *ACS Nano*, 2017, **11**, 4731–4744.
18 H. Wu, G. Chan, J. W. Choi, I. Ryu, Y. Yao, M. T. McDowell, S. W. Lee, A. Jackson, Y. Yang and L. Hu, *Nat. Nanotechnol.*, 2012, **7**, 310.
19 N. Liu, J. Liu, D. Jia, Y. Huang, J. Luo, X. Mamat, Y. Yu, Y. Dong and G. Hu, *Energy Storage Mater.*, 2019, **18**, 165–173.
20 Y. Han, J. Zhou, T. Li, Z. Yi, N. Lin and Y. Qian, *Nano Res.*, 2018, **11**, 6294–6303.
21 C. Xu, Q. Hao and D. Zhao, *Nano Res.*, 2016, **9**, 908–916.
22 F. Guo, P. Chen, T. Kang, Y. L. Wang, C. H. Liu, Y. Shen, W. Lu and L. Chen, *Acta Phys.-Chim. Sin.*, 2019, **35**, 1365–1371.
23 X. Zhang, D. Kong, X. Li and L. Zhi, *Adv. Funct. Mater.*, 2019, **29**, 1806061.
24 Y. Tian, Y. An and J. Feng, *ACS Appl. Mater. Interfaces*, 2019, **11**, 10004–10011.
25 X. Guo, Y.-Z. Zhang, F. Zhang, Q. Li, D. H. Anjum, H. Liang, Y. Liu, C. Liu, H. N. Alshareef and H. Pang, *J. Mater. Chem. A*, 2019, **7**, 15969–15974.
26 P. Lv, H. Zhao, Z. Li, C. Gao and Y. Zhang, *Solid State Ionics*, 2019, **340**, 115024.
27 K. W. Kim, H. Park, J. G. Lee, J. Kim, Y.-U. Kim, J. H. Ryu, J. J. Kim and S. M. Oh, *Electrochim. Acta*, 2013, **103**, 226–230.
28 T. Meng, B. Li, C. Liu, Q. Wang, D. Shu, S. Ou, M. S. J. T. Balogun, H. Su and Y. Tong, *Energy Storage Mater.*, 2022, **46**, 344–351.
29 A. Raza, J.-Y. Bang, H.-Y. Kim, J.-H. Choi, H.-Y. Choi and S.-M. Lee, *Sci. Technol. Adv. Mater.*, 2025, **26**, 2485868.
30 G. Xu, C. Jin, Y. Lan, L. Liu, K. Kong, X. Yang, Z. Yue, X. Li, F. Sun and H. Huang, *Mater. Lett.*, 2018, **233**, 228–232.
31 J. Zhang, J. Zhang, T. Bao, X. Xie and B. Xia, *J. Power Sources*, 2017, **348**, 16–20.
32 Y. Xu, Y. Li, Y. Qian, S. Sun, N. Lin and Y. Qian, *Inorg. Chem. Front.*, 2023, **10**, 1176–1186.
33 Y. Li, G. Chen, W. Liu, L. Huang and X. Luo, *Waste Manage.*, 2023, **156**, 22–32.
34 P. Ouyang, C. Jin, G. Xu, X. Yang, K. Kong, B. Liu, J. Dan, J. Chen, Z. Yue and X. Li, *Ceram. Int.*, 2021, **47**, 1086–1094.
35 D. Kim, J. Han, O.-S. Jung and Y.-A. Lee, *RSC Adv.*, 2022, **12**, 25118–25122.
36 Y. Liu, G. Ji, J. Wang, X. Liang, Z. Zuo and Y. Shi, *Nanoscale Res. Lett.*, 2012, **7**, 663.
37 B. M. Bang, J.-I. Lee, H. Kim, J. Cho and S. Park, *Adv. Energy Mater.*, 2012, **2**, 878–883.
38 W. An, B. Gao, S. Mei, B. Xiang, J. Fu, L. Wang, Q. Zhang, P. K. Chu and K. Huo, *Nat. Commun.*, 2019, **10**, 1447.
39 J. Wang, L. Liao, H. R. Lee, F. Shi, W. Huang, J. Zhao, A. Pei, J. Tang, X. Zheng and W. Chen, *Nano Energy*, 2019, **61**, 404–410.
40 F. Xi, Z. Zhang, X. Wan, S. Li, W. Ma, X. Chen, R. Chen, B. Luo and L. Wang, *ACS Appl. Mater. Interfaces*, 2020, **12**, 49080–49089.
41 Y. Zhong, X. Qiu, J. Gao and Z. Guo, *ISIJ Int.*, 2019, **59**, 1098–1104.
42 G. Zou, Z. Zhang, J. Guo, B. Liu, Q. Zhang, C. Fernandez and Q. Peng, *ACS Appl. Mater. Interfaces*, 2016, **8**, 22280–22286.
43 A. R. Iarchuk, V. A. Nikitina, E. A. Karpushkin, V. G. Sergeyev, E. V Antipov, K. J. Stevenson and A. M. Abakumov, *ChemElectroChem*, 2019, **6**, 5090–5100.
44 X. Lu, N. Zhang, M. Jahn, W. Pfleging and H. J. Seifert, *Appl. Sci.*, 2019, **9**, 3671.
45 A. Raza, F. Ghani, J. Lim, I. W. Nah and H.-S. Kim, *Microporous Mesoporous Mater.*, 2021, **314**, 110853.